Chapter 2
Modelling Orbital Dynamics in the Potential of Small Bodies

Abstract The research of orbital dynamics highly relies on the preliminary modelling work of target system, and an appropriate model comes from full understanding of the physics of the system. Two remarkable features of the dynamics problem around a small body should be noticed: first, the influences of different kinds of perturbations become relatively strong since the gravity from the small body is usually weak; second, the gravitational field of a real asteroid could be geometrically complex due to its irregular shape. Starting from these two points, this chapter discusses the modelling issues of orbital dynamics around a small body. An analysis of the perturbation magnitudes is presented first, and then described is the numeric methods to approximate the gravity from a small body. We compare these methods and show the advantages and disadvantages, respectively. Section 2.4 discusses about the orbital equations in the gravitational field of a small body. The basic form of the equation is first presented with the potential described by a homogenous polyhedron, and several transformations are listed to identify the general properties of this kind of systems, which is taken as the beginning to understand the following chapters. Section 2.5 deduces the unitless form of the motion equations and proposes a basic dynamical factor κ. Through qualitative analysis and numerical verifications of specific asteroids, we show this factor has a crucial influence on the global scheme of the orbital behaviors. Reference values of κ are listed for some real Solar System small bodies.

Keywords Extended body · Gravity · Reference systems · Integrability · Hamiltonian systems · Planets and satellites · Fundamental parameters

2.1 Introduction

The research of orbital dynamics highly relies on the preliminary modelling work of target system, and an appropriate model comes from full understanding of the physics of the system. Two remarkable features of the dynamics problem around an small body should be noticed: first, the influences of different kinds of perturbations become relatively strong since the gravity from the small body is usually weak;

second, the gravitational field of a real asteroid could be geometrically complex due to its irregular shape. Starting from these two points, this chapter discusses the modelling issues of orbital dynamics around a small body. An analysis of the perturbation magnitudes is presented first, and then described is the numeric methods to approximate the gravity from a small body. We compare these methods and show the advantages and disadvantages, respectively.

Section 2.4 discusses about the orbital equations in the gravitational field of a small body. The basic form of the equation is first presented with the potential described by a homogenous polyhedron, and several transformations are listed to identify the general properties of this kind of systems, which is taken as the beginning to understand the following chapters.

Section 2.5 deduces the unitless form of the motion equations and proposes a basic dynamical factor κ. Through qualitative analysis and numerical verifications of specific asteroids, we show this factor has a crucial influence on the global scheme of the orbital behaviours. Reference values of κ are listed for some real Solar System small bodies.

2.2 Mechanical Environment in the Vicinity of Small Bodies

About 90 % of known small bodies locate at the main asteroid belt which is roughly between the orbits of the planets Mars and Jupiter, $2.17 \sim 3.64$ AU away from the Sun. A major part of remained 10 % small bodies belong to near-Earth objects (NEOs), which are widely concerned because of their potential hazard to the Earth. NEA observing plans like Lincoln Near-Earth Asteroid Research (LINEAR) and Near-Earth Asteroid Tracking (NEAT) have monitored these small bodies for long terms [1]. According to the orbital features, NEAs are generally divided into three categories: Amor asteroids, whose orbits approach but do not cross Earth orbit, and whose orbits are further from the Sun than Earth's orbit (e.g., Eros); Apollo asteroids, whose orbits cross Earth's orbit, within Mars' orbit, and some of which have high eccentricities (e.g., 1892 Apollo); Aten asteroids, whose orbits also cross Earth's orbit, but unlike Apollos, Atens spend most of their time inside Earth orbit (e.g., 2062 Aten).

Since the number of Solar System small bodies is tremendous, their orbits are widely distributed, we are in lack of knowledge about the real spatial environment around them to date. Among the known perturbations, the gravitational perturbations from the Sun and planets, the solar radiation pressure and collisions from ejected debris and dust (from meteorite impacts) may have significant effects on the short-term motion of spacecraft. This section will not involve the influence of ejecta collision due to its randomness and uncertainty. Rather, we pay attention to more general perturbation forms, the third-body gravitational perturbation and solar radiation pressure.

The research on the effects of planetary gravity can date back to 1866, when American astronomer Kirkwood found the narrow gaps in the distribution of the

Fig. 2.1 The semi-major axis distribution of main-belt asteroids and Kirkwood gaps
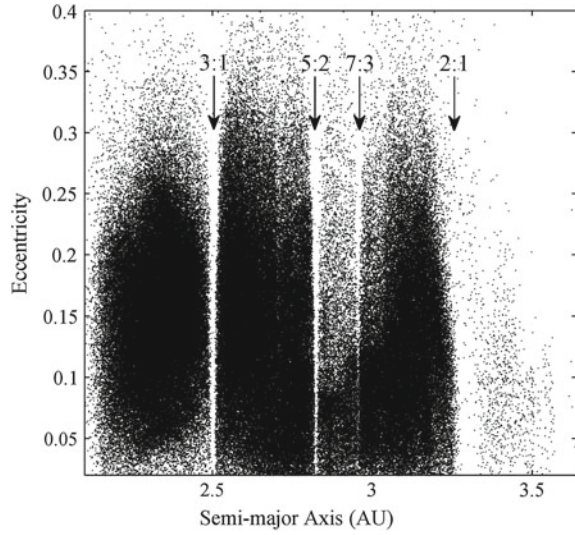
semi-major axis of the orbits of main-belt asteroids (named Kirkwood Gap) [2], as illustrated in Fig. 2.1. These gaps are resulted from the orbital resonances with Jupiter, which has cleared the asteroids out of these regions over a long term. All asteroids with orbital distances that form a simple ratio with that of Jupiter will be affected by such gravitational perturbations, e.g., the gaps occur at the 2:1, 3:1, 5:2 and 7:3 orbital resonances.

Similarly, the 1:1 resonance with Jupiter leads to a clearance effect on the objects running on its orbit, which are finally concentrated around the L_4, L_5 Lagrange points of Sun–Jupiter system, called Jupiter Trojan asteroids. Accordingly, Trojans have also been found at the L_4, L_5 of Earth, Mars and Uranus. Thus the effects of orbital resonance could be significant from a secular perspective, while in the work of this thesis, the time span of our concern is much shorter (days to months). Reference [3] confirmed the solar tide is the major perturbation in our case, and the planetary influence can be ignored for the study of short-term motion.

The acceleration of a mass point orbiting around a small body can be represented as

$$\frac{d^2}{dt^2}r \approx a + a_s + a_\odot, \tag{2.1}$$

where r indicates the position vector of the mass point, a indicates the gravitational acceleration from the small body, a_s indicates the acceleration of solar radiation pressure, and $a_\odot$ indicates the solar tidal acceleration. Equation 2.1 presents two major forms of perturbations, solar radiation pressure and solar tide. We will analysis the order of magnitudes of these perturbations. Formula 2.2 presents the general definition of the radius of influential sphere of a small body.

$$R = D \left(\frac{M_A}{M_\odot} \right)^\alpha, \tag{2.2}$$

in which, D is the mean distance from the small body to the Sun, M_A, $M_\odot$ are the masses of the small body and the Sun, respectively. The exponent parameter α discriminates the boundaries of these spherical regions. Equation 2.3 gives three common ways to define the radius R: $\alpha = 1/3$ corresponds to R_1, which is like the definition of Hill Sphere, meaning the magnitude of the solar tide equals to the small body's gravity at the boundary; $\alpha = 2/5$ corresponds to R_2, which is the classical definition of Sphere of Influence in astrodynamics, describes the boundary of the region in which the dominant gravity on an orbiting object is from the small body; $\alpha = 1/2$ corresponds to R_3, which means the magnitude of the solar gravity equals to that from the small body at the boundary.

$$R = \begin{cases} R_1 & \alpha = 1/3 \\ R_2 & \alpha = 2/5 \\ R_3 & \alpha = 1/2 \end{cases} \tag{2.3}$$

According to Eq. 2.3, $R_1 > R_2 > R_3$. Table 2.1 lists the values of these three radii for 23 asteroids with the latest mass information. The maximum radius R_1 is usually hundreds of times than the size of the asteroid, and the minimum radius R_3 is only tens of times, which is a strict estimation of the range dominated by the asteroid.

Hamilton et al. studied the orbital stability of natural satellites of the small bodies, and suggested that Hill radius can be used to estimate the region where a satellite might exist, i.e., the asteroidal gravity dominates the orbital motion within this region [3]. We compare the magnitudes of solar tide and solar radiation pressure at the boundaries of the spherical regions defined above. Equation 2.4 presents the dimensionless solar tide and solar radiation pressure, scaled by the asteroidal gravity. Combining Eq. 2.2, the scaled perturbations depend on the mass ratio of the small body and the Sun like

$$a_s/a \approx \beta \frac{GM_\odot}{D^2} \bigg/ \frac{GM_A}{R^2} = \beta \left(\frac{M_A}{M_\odot} \right)^{2\alpha-1},$$

$$a_\odot/a \approx \frac{R}{D} \frac{GM_\odot}{D^2} \bigg/ \frac{GM_A}{R^2} = \left(\frac{M_A}{M_\odot} \right)^{3\alpha-1}. \tag{2.4}$$

In which a, a_s, $a_\odot$ indicate the magnitudes of $\boldsymbol{a}$, $\boldsymbol{a}_s$, $\boldsymbol{a}_\odot$, respectively. β is the ratio of the radiation pressure force to the gravitational force of the Sun [4], and in our analysis, we only need to apply the general magnitude of β for a spacecraft. According to Ref. [5], we adopt $\beta = 3.37 \times 10^{-4}$. The scaled mass of known small bodies $M_A/M_\odot$ ranges from 5.03×10^{-21} to 4.74×10^{-10} due to Table 2.1. Figure 2.2 shows the magnitudes of scaled solar tide (a) and solar radiation pressure (b) over this range at R_1, R_2 and R_3, respectively. The value above 10^0 indicates the perturbation is greater than the gravity, and that below 10^0 indicates the perturbation is smaller

Table 2.1 The values of R_1, R_2 and R_3 for some asteroids

Asteroid	$M_A/M_\odot$	R_1 (km)	R_2 (km)	R_3 (km)
1 Ceres	4.81×10^{-10}	2.25×10^5	7.77×10^4	9.09×10^3
2 Pallas	1.00×10^{-10}	1.33×10^5	4.15×10^4	4.15×10^3
4 Vesta	1.38×10^{-10}	1.27×10^5	4.02×10^4	4.15×10^3
10 Hygiea	5.60×10^{-11}	1.25×10^5	3.72×10^4	3.51×10^3
11 Parthenope	2.56×10^{-12}	3.48×10^4	8.47×10^3	5.87×10^2
15 Eunomia	1.20×10^{-11}	6.27×10^4	1.69×10^4	1.37×10^3
16 Psyche	9.00×10^{-12}	6.30×10^4	1.67×10^4	1.31×10^3
20 Massalia	2.44×10^{-12}	3.36×10^4	8.16×10^3	5.63×10^2
45 Eugenia	3.00×10^{-12}	4.07×10^4	1.00×10^4	7.05×10^2
52 Europa	2.60×10^{-11}	9.52×10^4	2.70×10^4	2.36×10^3
87 Sylvia	7.60×10^{-12}	7.13×10^4	1.87×10^4	1.44×10^3
88 Thisbe	7.00×10^{-12}	5.49×10^4	1.43×10^4	1.10×10^3
90 Antiope	4.14×10^{-13}	2.44×10^4	5.27×10^3	3.04×10^2
121 Hermione	4.70×10^{-12}	5.99×10^4	1.52×10^4	1.12×10^3
216 Kleopatra	2.33×10^{-12}	1.98×10^4	3.33×10^3	2.28×10^3
243 Ida	2.20×10^{-14}	8.32×10^3	1.47×10^3	6.35×10^1
253 Mathilde	5.19×10^{-14}	1.02×10^4	1.92×10^3	9.02×10^1
433 Eros	3.60×10^{-15}	2.32×10^3	3.64×10^2	1.31×10^1
444 Gyptis	4.00×10^{-12}	4.56×10^4	1.14×10^4	8.29×10^2
511 Davida	5.60×10^{-11}	1.26×10^5	3.75×10^4	3.54×10^3
704 Interamnia	3.50×10^{-11}	1.04×10^5	3.01×10^4	2.71×10^3
762 Pulcova	1.28×10^{-12}	3.56×10^4	8.26×10^3	5.34×10^2
766391 1999KW4	1.10×10^{-18}	6.88×10^1	6.30×10^0	1.01×10^{-1}

than the gravity. To make sense of the variation of perturbations with the mass, three typical asteroids are marked on the curves in Fig. 2.2, including Vesta ($\sim$525.4 km), Eros ($\sim$16.8 km) and 1999KW4 ($\sim$1.4 km).

Figure 2.2 shows both solar radiation pressure and solar tide can not be neglected for the study of orbital motion beyond R_1, when the former is greater than the gravity, and the latter is equivalent with the gravity. And at a distance of R_2, solar tide is ignorable, and the relative effect of solar radiation pressure depends on the mass of small body: it is ignorable for big objects like Vesta, and considerable for smaller ones like Eros. At a distance of R_3, the solar tide perturbation is smaller than that of solar radiation pressure, which is much smaller than the gravity. Therefore, we confirm the gravity of the small body is the dominant force governing the motion within the spherical region of radius R_3 (usually tens of the small body's diameter), when the perturbations of solar tide and solar radiation pressure are negligible for short-term orbital motion.

Fig. 2.2 The magnitudes of scaled perturbations varying as the mass of the small body. **a** Solar radiation pressure. **b** Solar tide
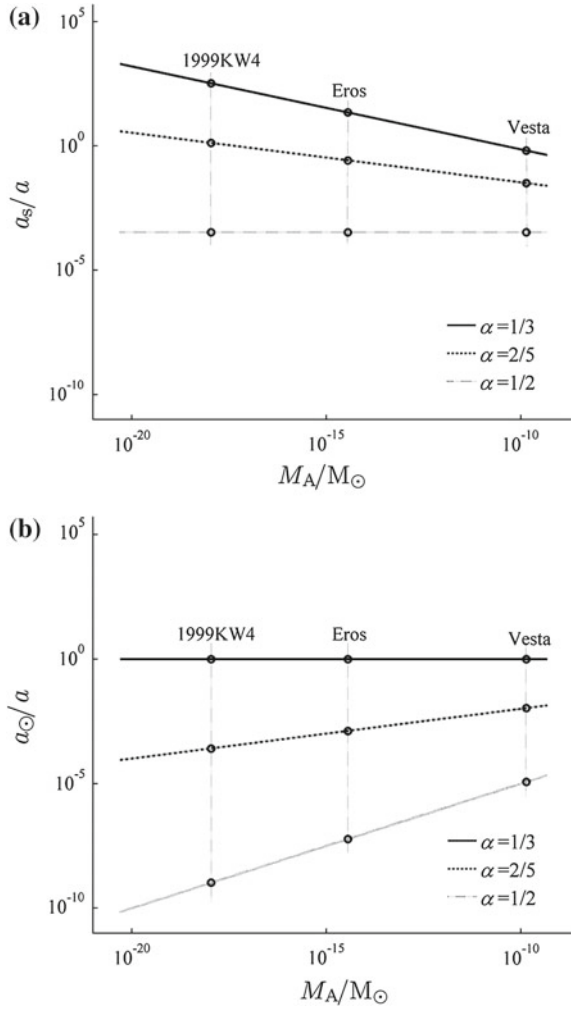
2.3   Descriptions of the Gravitational Field

Solar system small bodies are composed of meteorite material, and their masses are usually small so that the gravity is quite weak, which is insufficient to maintain a spherical overall shape against the interior strength. Thus differing from planets, small bodies are various in shape and most of them have irregular outlooks and pockmarks on the surface due to meteorite impacts (Fig. 2.3). Besides, the interior structures of the small bodies, as well as the surface landforms, have also been modified by different kinds of weathering mechanisms in space. It is an established fact that most asteroids have "rubble pile" structures, i.e. aggregates of rocks gathered
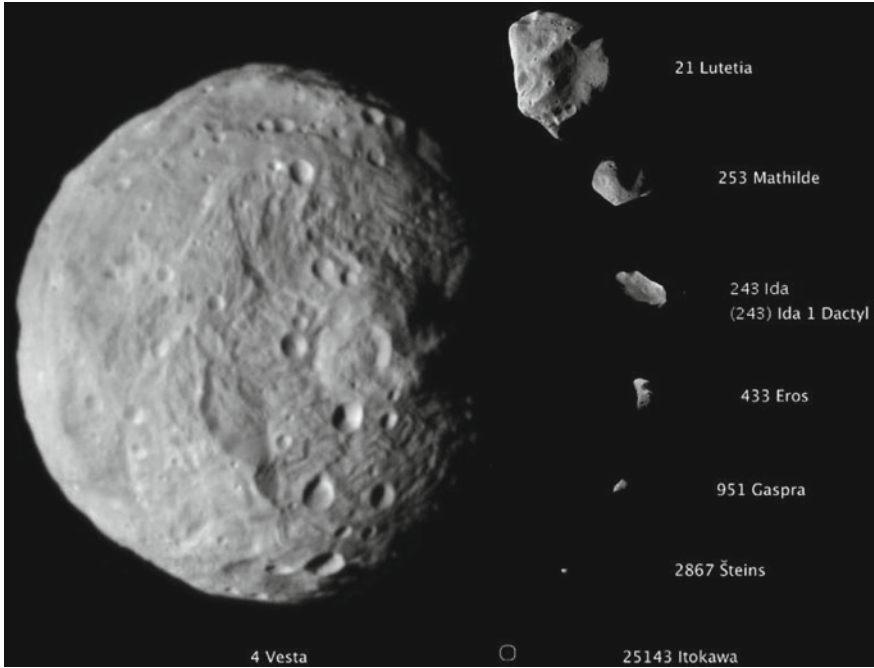
Fig. 2.3 Some small bodies with images of high resolution (scaled in equal proportion). Reprinted from Ref. [6], copyright 2015 by NASA

only by their mutual gravities. All these matters contribute to asymmetric and irregular gravitational field around the small bodies, therefore to choose an appropriate method to describe the gravity is a crucial work for the study orbital dynamics near the small bodies.

2.3.1 Mass Point Cluster

Mass point cluster (also known as "mascon") is a direct method to approximate the gravitational field of arbitrary object. According to this method, a small body is discretised into a series of voxels, and the gravity/potential from each of these voxels can be estimated using a mass point locating at its centre. Then the sum of the unit gravity/potential from all voxels will be taken as the result from the target object.

Particularly, consider a division of N voxels. $\mathbf{d}_i$, M_i indicate the position and the mass of ith voxel, respectively. The gravitational acceleration from the target body can be represented as

$$\mathbf{a} = \sum_{i=1}^{N} \frac{GM_i \left(\mathbf{r} - \mathbf{d}_i\right)}{\left|\mathbf{r} - \mathbf{d}_i\right|^3}, \tag{2.5}$$

where the voxel mass M_i subject to

$$\sum_{i=1}^{N} M_i = M_A, \tag{2.6}$$

and the gravitational potential from the unit voxel is

$$U = \sum_{i=1}^{N} \frac{GM_i}{|\boldsymbol{r} - \boldsymbol{r}_i|}. \tag{2.7}$$

The method of mass point cluster has several obvious advantages. First, the algorithm is simple and operable; and second, its convergence is evident that the approximate accuracy increases as the number of voxels N [7]; third, this method is quite portable to the real states of an asteroid, e.g. for asteroids of rubble pile interiors, the arrangement of the voxels in the cluster can be alternated with a meshless scheme, and the mass of the voxels M_i can be conveniently modified to fit the nonuniform distribution of the density of a real small body.

Figure 2.4 shows the stated advantages with an example solid ellipsoid of triaxial ratio 0.8:1.0:0.4 (a). A uniform division of about 1, 000 equal-sized spherical voxels is shown in Fig. 2.4b, which is achieved using hexagonal close packing, i.e. a pattern of the best space utilization rate for equal-sized spheres. Figure 2.4c shows a division of bimodal-sized spherical voxels in meshless packing which is achieved by randomly piling these spheres up in a natural way.

The method of mass point cluster has been successfully applied to the analysis of binary motion, and Llanos et al. applied it to their studies of an ESA sampling mission concept, which involves the hovering control of spacecraft near the target asteroid 341843 2008EV5 based on a gravitational field model.

In spite of the great potential in applications, the method of mass point cluster does not perfectly fit for our problem: first, the convergence of this method is quite slow, and the calculated amount increases rapidly as the voxel number of the division; second, Eqs. 2.5 and 2.7 indicate great cumulated errors for the terms within the sum, which could be another obstacle during practical calculation; third, as the study of orbital motion near a small body, an issue that cannot be avoided is collision detection, which is to find out whether the object has entered inside the body, however, this method provides no efficient information about that, and a collisional routine must be employed in parallel, which will cost computational wastes.

2.3.2 Spherical/Ellipsoidal Harmonics

The method of spherical harmonics is mature and efficient in describing the gravitational field of planets, which is widely used in the study of orbital dynamics
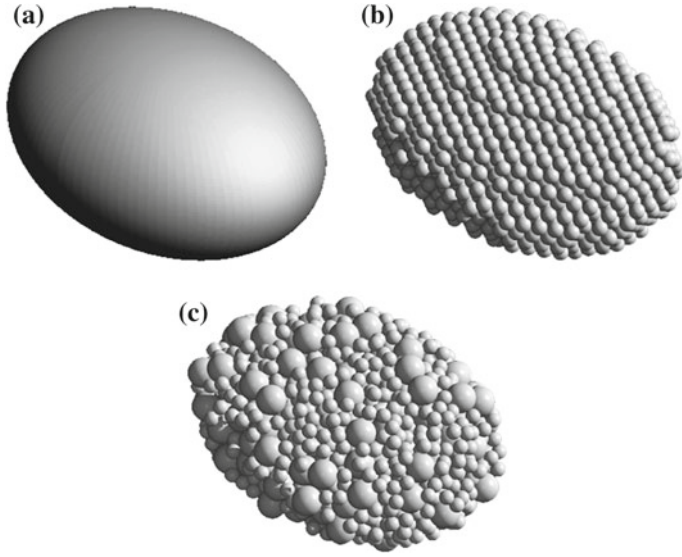
Fig. 2.4 Divisions to an ellipsoid with the method of mass point cluster. **a** Solid triaxial ellipsoid. **b** Uniform division of equal-sized voxels. **c** Meshless division of bimodal-sized voxels

of man-made satellite. As a general approach, it also applies to the non-spherical perturbations of gravitational field around a small body. Equation 2.8 presents the expansion of the potential at a massless mass point by spherical harmonics.

$$U = \frac{GM_A}{r} \left\{ 1 + \sum_{n=1}^{\infty} \sum_{m=0}^{n} \left(\frac{r_e}{r} \right)^n P_{nm} \left(\sin\varphi \right) \left[C_{nm} \cos m\lambda + S_{nm} \sin m\lambda \right] \right\}, \quad (2.8)$$

in which r, φ and λ are the spherical coordinates of the mass point, P_{nm} indicate associated Legendre polynomials, and C_{nm}, S_{nm} are the coefficients of spherical harmonics, representing the non-spherical terms of the gravitational field. r_e indicates the radius of the reference sphere, defining the convergence domain, i.e. Eq. 2.8 fails inside the reference sphere. Since there is no explicit expression of the mass distribution inside the small body, the coefficients C_{nm} and S_{nm} can not be derived directly by integration. The estimation of these coefficients is the major part of gravitational field modelling, and the common approaches involve inversion from the flight data and approximation through the body's shape and density.

The method of ellipsoidal harmonics is an improved version of the spherical harmonics, aiming at better approximation to the irregular gravitational fields. Equation 2.9 presents the expansion of the potential at a massless mass point by ellipsoidal harmonics.

$$U = GM_A \sum_{n=0}^{\infty} \sum_{m=1}^{2n+1} \alpha_{nm} \frac{F_{nm}(\lambda_1)}{F_{nm}(\lambda_e)} F_{nm}(\lambda_2) F_{nm}(\lambda_3), \quad (2.9)$$

where $\lambda_1, \lambda_2, \lambda_3$ are orthogonal ellipsoidal coordinates [8], λ_e indicates the reference ellipsoid (or Brillouin ellipsoid), which defines the convergence domain of Eq. 2.9. F_{nm} are the canonical solutions to Lamé equation, which are continuous functions when $\lambda_1 \geq \lambda_e$. α_{nm} indicate ellipsoidal coefficients. The corresponding gravity forms of these two methods are determined by gradients of Eqs. 2.8 and 2.9, respectively.

Figure 2.5 illustrates a comparison between the convergence domains of these two methods about asteroid Castalia. Since Castalia has a dumbbell-like shape, Fig. 2.5a shows the reference sphere employed in the spherical harmonics, which excludes a large area around Castalia that may be traversed by the orbits; and Fig. 2.5b shows the reference ellipsoid, which fits the overall shape of Castalia better and widens the convergence domain of the gravitational formulas.

As shown in Fig. 2.5, the method of ellipsoidal harmonics has some sort of advantage in describing the gravitational field of a small body, and it has been successfully applied to fitting the gravity data of Eros returned by NEAR Shoemaker [9], and the method of spherical harmonics, which is usually used together with the polyhedral method (see Sect. 2.3.3), works well for the orbital segments far from the small body and is efficient in computing. While a common disadvantage of the methods of harmonics is the convergence that depends on the distance away from the central body, i.e. the closer to the boundary of convergence domain, the lower the approximating precision becomes. This essentially affects the global accuracy of this type of methods, because the close approaches to the small body is hard to avoid in our study of orbital dynamics. Besides, similarly as the mass point cluster, the methods of harmonics provide no clues to collision detection, and to make it works, a parallel collisional routine will be necessary.
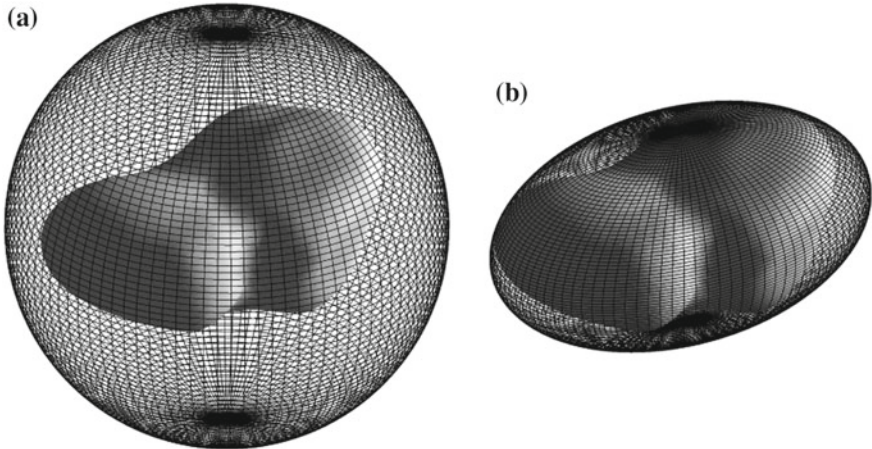

Fig. 2.5 The reference sphere and ellipsoid about asteroid 4769 Castalia. **a** Reference sphere of spherical harmonics. **b** Reference ellipsoid of ellipsoidal harmonics

2.3.3 Polyhedral Method

The polyhedral method applied in geological modelling can date back to the early time, but it was only applied in describing the small body's shape and calculating the gravity as late as twenty-nineties. Werner et al. derived the expressions of the gravitational potential, attraction and gradient matrix of a homogenous polyhedron based on dyads of the second order [10], which is known as the classic polyhedral method to describe the irregular gravitational field of a small body, and we take it as the major tool to construct the field model of the target small body in this thesis.

The rest of this section will present some fundamentals of the polyhedral method, in order to construct the gravitational model of a small body. Figure 2.6 shows a tetrahedron as the simplest example of arbitrary polyhedron P of a uniform bulk density σ. The potential induced by P at any position of its exterior r is

$$U = G\sigma \iiint_P \frac{1}{r} dV. \tag{2.10}$$

By applying Gaussian divergence theorem to Eq. 2.10, we have Eq. 2.11.

$$U = \frac{1}{2} G\sigma \sum_{f \in FS} \hat{\boldsymbol{n}}_f \cdot \boldsymbol{r}_f \iint_f \frac{1}{r} dS, \tag{2.11}$$

where $\hat{\boldsymbol{n}}_f$ is the outwarding normal vector of facet f, as shown in Fig. 2.6, and the hat symbol ˆ indicates a unit vector in this thesis. $\boldsymbol{r}_f$ indicates the vector from r to any point on the facet f, and FS indicates the set of all facets of P. Then the areal integral term in Eq. 2.11 can be written as

$$\iint_f \frac{1}{r} dS = \sum_{e \in ES_f} L_e^f \boldsymbol{r}_e^f \cdot \hat{\boldsymbol{n}}_e^f - \theta_f \hat{\boldsymbol{n}}_f \cdot \boldsymbol{r}_f, \tag{2.12}$$

Fig. 2.6 The tetrahedron as an example of the polyhedral method
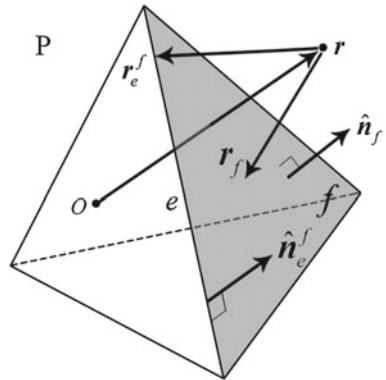
in which L_e^f indicates the line integral term about the edge e of facet f, θ_f is the solid angle corresponding to facet f whose sign is defined as: $\theta_f > 0$ if $\boldsymbol{r}_f \cdot \boldsymbol{n}_f < 0$; $\theta_f = 0$ if $\boldsymbol{r}_f \cdot \boldsymbol{n}_f = 0$; $\theta_f < 0$ if $\boldsymbol{r}_f \cdot \boldsymbol{n}_f > 0$. Besides, $\boldsymbol{r}_e^f$ indicates the vector from $\boldsymbol{r}$ to any point on the edge e, and $\hat{\boldsymbol{n}}_e^f$ indicates the outwarding unit vector of edge e, lying inside the plane of facet f. ES_f is the set of the all edges of facet f. Then substituting Eq. 2.12 into Eq. 2.11, we have

$$U = \frac{1}{2}G\sigma \sum_{f \in FS} \sum_{e \in ES_f} L_e^f \boldsymbol{r}_f \cdot \hat{\boldsymbol{n}}_f \hat{\boldsymbol{n}}_e^f \cdot \boldsymbol{r}_e^f - \frac{1}{2}G\sigma \sum_{f \in FS} \theta_f \boldsymbol{r}_f \cdot \hat{\boldsymbol{n}}_f \hat{\boldsymbol{n}}_f \cdot \boldsymbol{r}_f. \quad (2.13)$$

Equation 2.13 can be simplified by reducing the terms of common edges of adjacent facets. For instance, e is the common edge of facet f_1 and facet f_2. By introducing the dyad $\mathbf{E}_e = \hat{\boldsymbol{n}}_{f_1}\hat{\boldsymbol{n}}_e^{f_1} + \hat{\boldsymbol{n}}_{f_2}\hat{\boldsymbol{n}}_e^{f_2}$ and the dyad $\mathbf{F}_f = \hat{\boldsymbol{n}}_f\hat{\boldsymbol{n}}_f$, and by noticing $L_e^{f_1} = L_e^{f_2}$ (unified as L_e) and $\boldsymbol{r}_f \cdot \hat{\boldsymbol{n}}_f = \boldsymbol{r}_e^f \cdot \hat{\boldsymbol{n}}_f$, Eq. 2.13 turns into

$$U = \frac{1}{2}G\sigma \left(\sum_{e \in ES} L_e \boldsymbol{r}_e \cdot \mathbf{E}_e \cdot \boldsymbol{r}_e - \sum_{f \in FS} \theta_f \boldsymbol{r}_f \cdot \mathbf{F}_f \cdot \boldsymbol{r}_f \right), \quad (2.14)$$

in which ES indicates the set of all edges of the polyhedron P. Equation 2.14 presents a closed form of the potential in the exterior of P, and accordingly the gradient and gradient tensor of Eq. 2.14 determine the gravity and its gradient matrix, respectively, as shown in Eqs. 2.15 and 2.16 (see Ref. [10] for more details).

$$\nabla U = -G\sigma \left(\sum_{e \in ES} L_e \mathbf{E}_e \cdot \boldsymbol{r}_e - \sum_{f \in FS} \theta_f \mathbf{F}_f \cdot \boldsymbol{r}_f \right), \quad (2.15)$$

$$\nabla\nabla U = G\sigma \left(\sum_{e \in ES} L_e \mathbf{E}_e - \sum_{f \in FS} \theta_f \mathbf{F}_f \right). \quad (2.16)$$

The advantages of polyhedral method are obvious: first, the closed forms of Eqs. 2.14–2.16 avoid truncation errors during the computing, i.e. the major part of the errors comes from modelling precess (e.g., the bias of estimation for the shape and density distribution), and the accuracy of the polyhedral method is compatible with the resolution of the polyhedron employed as the shape model; second, differing from the methods of harmonics, the approximating precession of polyhedral method does not depend on the distance away from the small body, which is uniformly effective at places even close to the polyhedron; third, this method enables a quick and convenient judgement of whether a point has entered the interior of a polyhedron P, i.e. recalling the sum of all solid angles Ω as defined in Eq. 2.17, the position of the point $\boldsymbol{r}$ lies inside P if $\Omega = 4\pi$, else $\Omega = 0$.

$$\Omega = \sum_{f \in FS} \theta_f. \tag{2.17}$$

In addition, the polyhedral method based on the target's shape is well suited to the practical mission, that during the approaching segment, the shape model of target small body is obtained firstly by optical measurement, based on which a preliminary gravity model can be built using this method. This model will contribute to the early approaching operations, which are of high risks since the dynamical environment has not been well understood. Then the flight data of the spacecraft will be analyzed, tending to build a more accurate gravity model.

We prefer the polyhedral method and take it as the major methodology in this study because it can provide good approximation close to the surface of an irregular body. However, it is notable the advantage is not unique, e.g. the methods of harmonics could be much more computationally efficient than the polyhedral method when the spacecraft is far away from the target body (say tens of times of its radius).

2.4 Motion Equations

The motion equations of a test mass point in the vicinity of a small body (within radius R_3) are given in this section, considering the irregular gravitational field calculated with the polyhedral method. The vectors of the small body's angular velocity and acceleration are denoted by $\boldsymbol{\omega}$ and $\boldsymbol{\alpha}$, respectively, and frames are defined as follows (Fig. 2.7):

1. Mass centre inertia frame $OXYZ$: a translational frame with the origin at the mass centre of the small body O, axis X pointing at J2000 mean equinox, XY plane parallel with the Earth's orbital plane, and axes Z, Y, X forming a right-handed system.
2. Mass centre body-fixed frame $Oxyz$: the origin locates at the mass centre O, and axes x, y, z indicate the principal axes of minimum, medium, maximum inertia, respectively, forming a right-handed system.

Considering a massless point, i.e. the gravity from the mass point has no influence on the small body, the motion equation of the mass point is
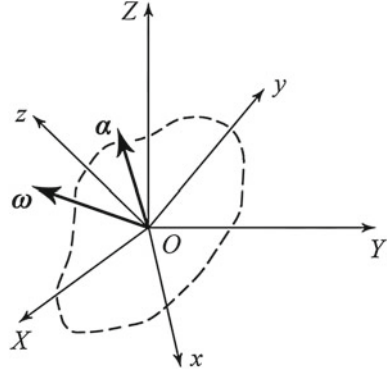
$$\frac{\mathrm{d}^2}{\mathrm{d}t^2}\boldsymbol{r} = -\nabla U. \tag{2.18}$$

Then the left hand side of Eq. 2.18 represented in relative derivatives yields

$$\ddot{\boldsymbol{r}} + 2\boldsymbol{\omega} \times \dot{\boldsymbol{r}} + \boldsymbol{\omega} \times (\boldsymbol{\omega} \times \boldsymbol{r}) + \boldsymbol{\alpha} \times \boldsymbol{r} = -\nabla U, \tag{2.19}$$

where "d/dt" indicates the absolute derivative about time t, and "˙" indicates the relative derivative about t. Furthermore, most of the small bodies are supposed to be

Fig. 2.7 The frames and
rotational vectors of a small
body

rotating around the principal axis, and the variation of angular velocity is quite slow
[11]. Approximately we assume $\boldsymbol{\alpha} = \boldsymbol{0}$, Eq. 2.19 turns into

$$\ddot{\boldsymbol{r}} + 2\boldsymbol{\omega} \times \dot{\boldsymbol{r}} + \boldsymbol{\omega} \times (\boldsymbol{\omega} \times \boldsymbol{r}) = -\nabla U, \tag{2.20}$$

Defining the efficient potential of a rotating body Eq. 2.21, we have a simplified
form of the motion equation Eq. 2.22.

$$V = -\frac{1}{2} (\boldsymbol{\omega} \times \boldsymbol{r}) \cdot (\boldsymbol{\omega} \times \boldsymbol{r}) + U, \tag{2.21}$$

$$\ddot{\boldsymbol{r}} + 2\boldsymbol{\omega} \times \dot{\boldsymbol{r}} = -\nabla V. \tag{2.22}$$

Equation 2.22 describes a complete system, including a Coriolis force term and
a potential force term, which is apparently also a conserved system. Define a state
variable $\boldsymbol{x}$ (Eq. 2.23), Eq. 2.22 is restated in a general form Eq. 2.24.

$$\boldsymbol{x} = \begin{bmatrix} \boldsymbol{r} \\ \dot{\boldsymbol{r}} \end{bmatrix}, \tag{2.23}$$

$$\dot{\boldsymbol{x}} = f(\boldsymbol{x}). \tag{2.24}$$

Introducing the canonical variables $\boldsymbol{q} = \boldsymbol{r}$, $\boldsymbol{p} = \boldsymbol{\omega} \times \boldsymbol{r} + \dot{\boldsymbol{r}}$, the Hamiltonian form
of system Eq. 2.24 is derived using Legendre transformation [12]:

$$\boldsymbol{q} = \frac{\partial H}{\partial \boldsymbol{p}}, \ \boldsymbol{p} = -\frac{\partial H}{\partial \boldsymbol{q}}, \tag{2.25}$$

in which H is the Hamiltonian function

$$H = \frac{1}{2} \boldsymbol{p} \cdot \boldsymbol{p} - (\boldsymbol{\omega} \times \boldsymbol{q}) \cdot \boldsymbol{p} + U. \tag{2.26}$$

The Hamiltonian function is independent on time t (Eq. 2.27), thus it determines a general energy integral C, called Jacobi integral.

$$\frac{\mathrm{d}}{\mathrm{d}t}H = 0. \tag{2.27}$$

The symplectic structure of system Eq. 2.25 forms the basis of understanding the orbital behaviours around the small body

1. Equation 2.25 has only one first integral C and has no cyclic coordinates;
2. Liouville theorem ensures the invariance of the infinitesimal phase space volume, namely there is no asymptotic behaviours in the flow field of such a system;
3. Liouville theorem also suggests all the stable periodic orbits of system Eq. 2.25 are of the critical case.

As an aside, we may refer to one of these forms of the motion equation as necessary (Eqs. 2.20, 2.22, 2.24 and 2.25) in following chapters of this thesis.

2.5 Dynamical Factor κ

In order to simplify the expressions, we present the dimensionless form of Eq. 2.20, taking the rotational period T_A as the time scaler $[T]$, and the equivalent radius (the radius of a sphere with the same volume) as the length scaler $[L]$ (Eq. 2.28).

$$[T] = T_A, \ [L] = \sqrt[3]{\frac{3V_A}{4\pi}}. \tag{2.28}$$

Introducing scaled time $\tau = t/[T]$, and combining Eqs. 2.15 and 2.20, we have

$$\tilde{r}'' + 4\pi\,\hat{\omega}\times\tilde{r} + 4\pi^2\hat{\omega}\times\left(\hat{\omega}\times\tilde{r}\right) = \kappa\left(\sum_{e\in ES}L_e\mathbf{E}_e\cdot\tilde{r}_e - \sum_{f\in FS}\theta_f\mathbf{F}_f\cdot\tilde{r}_f\right), \tag{2.29}$$

where "$'$" indicates the relative derivative about the scaled time τ, and "$\tilde{}$" indicates scaled length vectors. The dimensionless parameter on the right hand side of Eq. 2.29 is defined as

$$\kappa = \mathrm{G}T_A^2\sigma. \tag{2.30}$$

We regard κ as an important indicator for the orbital behaviours around the small body. The bracketed terms on the right hand side of Eq. 2.29 correspond to the polyhedral shape of the target small body, and κ is a comprehensive reflection of the influence of the small body's rotational period and bulk density, i.e. it describes the combination of the asteroidal gravity and centrifugal force due to the rotation.

Qualitatively, large κ value can respond to a large bulk density, or a slow rotational speed of the target body.

The dependence of the system dynamics on parameter κ is checked for a specific asteroid 433 Eros. Figure 2.8 show the polyhedral shape model of Eros, including 856 vertices and 1708 triangle facets. Eros has an elongated shape, with a narrow "neck" in the middle (supposed to be formed by a meteorite impact), box size of $11.87 \times 14.44 \times 32.74$ km. According to the data returned by NEAR Shoemaker, Eros has a bulk density of 2.67 g/cc, and is rotating uniformly around the principal axes of maximum inertia with the period 5.27 h.

Figure 2.9 illustrates the variation of efficient potential V on the equatorial plane as κ increasing, in which the contour lines of V are shown at $\kappa = 10$ (a), $\kappa = 30$ (b), $\kappa = 64$ (c) and $\kappa = 990$ (d), respectively. The singular points of the contour lines indicate the stationary values of function $V(x, y)$, or namely, the equilibrium points of gravity and centrifugal force (stationary orbit in inertia frame). As shown in Fig. 2.9, (a) when $\kappa = 10$, there exists only 1 equilibrium point in the exterior of Eros, which is close to the surface, suggesting a strong centrifugal effect that the surface material can cannot accumulate if there is no coherence force; (b) when $\kappa = 30$, the gravitational effect of Eros is stronger, and there appear 2 equilibrium points close to the surface; (c) when $\kappa = 64$ (close to the actual value of Eros 64.10), there are 4 equilibrium points (the 2 along the long axis are close to the surface), in which case the regolith material can stay on the surface of Eros relying on the gravity; (b) when $\kappa = 990$, the 4 equilibrium points are far away from Eros, showing the gravity is the dominant role in the near-field regime of Eros in this case.

The above discussion shows the altitude of stationary orbit (distance from the equilibrium to the surface of the small body) is a crucial indicator, which determines the dynamics of system to some extent. Here we give a general approximate analysis:

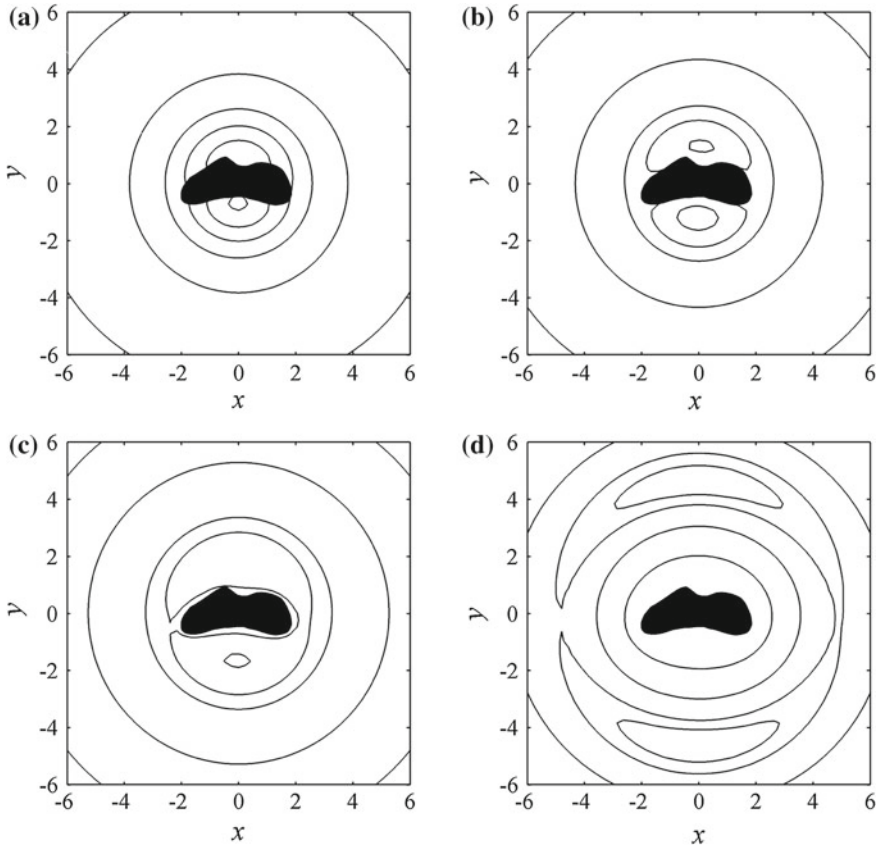**Fig. 2.8** The polyhedral shape model of asteroid 433 Eros
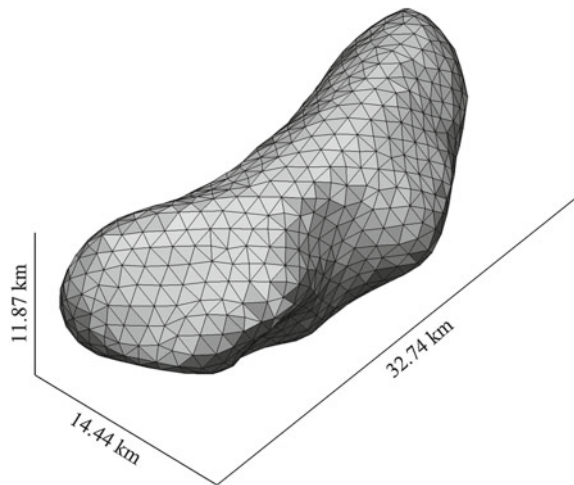
Fig. 2.9 The contour lines of efficient potential V on the equatorial plane of asteroid 433 Eros (plotted in scaled axes). **a** $\kappa = 10$. **b** $\kappa = 30$. **c** $\kappa = 64$ (close to the actual value). **d** $\kappa = 990$

assuming the target body is a solid sphere of radius $[L]$, the altitude of stationary orbit h satisfies

$$h = \left(\sqrt[3]{\frac{\kappa}{3\pi}} - 1 \right) [L].$$

(2.31)

According to Eq. 2.31, h and κ are correlated: $h \geq 0$ if $\kappa \geq 3\pi$, in which case the equilibrium points locate outside the target body, and divide the regions dominated by the gravity and that by the centrifugal force; $h < 0$ if $\kappa < 3\pi$, in which case the equilibrium points locate inside the target body, and the self-gravity of the body is not sufficient to hold the surface materials, which are aggregated by coherence force within the matter. Note that most Solar System small bodies (especially those of diameter greater than 300 m) have "rubble pile" interiors, therefore bodies of $\kappa < 3\pi$ should be quite rare in reality.

Table 2.2 The bulk densities, rotational periods and κ values of 24 asteroids

Asteroid	σ (g/cc)	T_A (h)	κ
1 Ceres	2.12	9.07	150.7583
2 Pallas	2.71	7.81	142.9999
4 Vesta	3.44	5.34	84.8588
10 Hygiea	2.76	27.62	1820.4620
11 Parthenope	2.72	9.43	209.0851
15 Eunomia	0.96	6.08	30.7070
16 Psyche	2.00	4.20	30.4391
20 Massalia	3.26	8.10	184.8009
22 Kalliope	2.50	4.15	37.1833
45 Eugenia	1.20	5.70	33.6907
87 Sylvia	1.62	5.18	37.6336
90 Antiope	1.30	16.50	305.9441
121 Hermione	1.96	6.00	60.9943
216 Kleopatra	3.60	5.39	90.2412
243 Ida	2.60	4.63	48.2632
253 Mathilde	1.30	8.17	75.0099
433 Eros	2.67	5.27	64.1008
704 Interamnia	4.40	8.69	287.2255
762 Pulcova	1.80	5.84	53.0494
804 Hispania	4.90	7.40	231.9479
1620 Geographos	2.00	5.22	47.1088
2063 Bacchus	2.44	14.90	468.2667
66391 1999KW4	2.39	2.77	15.7950
2000UG11	1.47	4.44	25.0504

Table 2.2 lists the κ values of 24 asteroids with known bulk densities and rotational periods. It shows the κ of these real small bodies distributes over a wide range from 15.79 to 1820.46, and over 70 % are concentrated within the range from 20 to 200. The results of all these 24 asteroids conform with $\kappa \geq 3\pi$, which supports the theory of "rubble pile" structure with solid evidences in dynamics.

2.6 Summary

This chapter discussed the methodologies of dynamic modelling for a spacecraft (or small natural objects) orbiting around a small body, and special attentions are paid to the mathematical essence and parameter dependence of the motion equations.

The first part of this chapter presents an analysis on two major forms of perturbations (solar radiation pressure and the solar tide), including the perturbative magnitudes varying as the mass of target body and the distance away from it. The near-field region dominated by the gravity of the small body is defined by recalling and comparing three typical definitions of the influential sphere. In the second part, this chapter surveyed the major approaches to describe the gravitational field of a celestial body, clarified the advantages of polyhedral method and discussed the probabilities to apply other approaches as supplement means.

We proposed a crucial dynamical factor κ and checked the dependence of system behaviours on it, showing the following points:

1. For a given shape model, the value of κ determines the geometric properties of the efficient potential V, whose topology changes as κ;
2. The value of κ determines the number and positions of the equilibrium points, and the spatial area dominated by the gravity of the small body;
3. All the asteroids we checked (with known bulk density and rotational period) satisfy $\kappa > 3\pi$, which supports the "rubble pile" structures of SSSBs in statistics.

References

1. NEAT (Near-Earth Asteroid Tracking). Issue (2014). available at http://neat.jpl.nasa.gov/
2. Bowell E, Virtanen J, Muinonen K (2002) Asteroid orbit computation. In: William F et al Asteroids III. University Arizona Press, Tucson, AZ, pp 27–44
3. Hamilton DP, Burns JA (1991) Orbital stability zones about asteroids. II. The destabilizing effects of eccentric orbits and of solar radiation. Icarus 96:43–64
4. Gong S (2009) Study on dynamics and control of sail-craft. Tsinghua University, Beijing
5. Chen Q, Chen Z, Wang H (2013) Method of modeling solar radiation pressure based on attitude control law of navigation satellites. In: 4th national satellite guidance academic annual conference, Wuhan, China, 15–18 May 2013
6. NASA (National Aeronautics and Space Administration). Issue (2015). available at http://www.nasa.gov/multimedia/imagegallery/image_feature_2010.html
7. Werner RA, Scheeres DJ (1997) Exterior gravitation of a polyhedron derived and compared with harmonic and mascon gravitation representations of asteroid 4769 castalia. Celest. Mech. Dyn. Astron. 65:313–344
8. Romain G, Jean-Pierre B (2001) Ellipsoidal harmonic expansions of the gravitational potential: theory and application. Celest. Mech. Dyn. Astron. 19:235–275
9. Garmier R, Barriot J, Konopliv AS et al (2002) Modeling of the Eros gravity field as an ellipsoidal harmonic expansion from the NEAR Doppler tracking data. Geophys Res Lett 29:721–723
10. Werner RA (1994) The gravitational potential of a homogeneous polyhedron or don't cut corners. Celest. Mech. Dyn. Astron. 59:253–278
11. Pravec P, Harris AW, Michalowski T (2002) Asteroid rotations. In: William F et al Asteroids III. University, Arizona Press, Tucson, AZ, pp 113–122
12. Arnold VI (2006) Mathematical methods of classical mechanics. In: Translated by Qi M (ed), vol 4, Higher Education Press, Beijing, pp. iii–v